POLITECNICO DI TORINO
Repository ISTITUZIONALE

Beyond 30 mW of Single-Mode Power in Linearly-Polarised VCSELs

Original
Beyond 30 mW of Single-Mode Power in Linearly-Polarised VCSELs / Torrelli, V., Gullino, A., Lindner, J., Moiso, G., Dalessandro, M., Gronenborn, S., Herper, M., Pusch, T., Moench, H., Tibaldi, A., Bertazzi, F., Goano, M., Alasio, M., Debernardi, P.. - In: IEEE JOURNAL OF SELECTED TOPICS IN QUANTUM ELECTRONICS. - ISSN 1558-4542. - STAMPA. - 32:6(2026), pp. 1-12. [10.1109/JSTQE.2026.3710026]

Availability:
This version is available at: 11583/3014187 since: 2026-08-08T05:58:16Z

Publisher:
IEEE

Published
DOI:10.1109/JSTQE.2026.3710026

Terms of use:

This article is made available under terms and conditions as specified in the corresponding bibliographic description in the repository

Publisher copyright

(Article begins on next page)

17 November 2026

Beyond 30 mW of Single-Mode Power in Linearly-Polarised VCSELs

Valerio Torrelli, Alberto Gullino, Julian Lindner, Gabriele Moiso, Martino D'Alessandro, Stephan Gronenborn, Markus Herper, Tobias Pusch, Holger Moench, Alberto Tibaldi, Francesco Bertazzi, Michele Goano, *Senior Member, IEEE*, Matteo C. G. Alasio, *Member, IEEE*, and Pierluigi Debernardi

(Invited Paper)

***Abstract*—We present a set of design rules for high-power single-polarisation-mode (SPM) vertical-cavity surface-emitting lasers (VCSELs) featuring an axial far-field (FF) intensity profile, and validate them through the fabrication and experimental characterization of dedicated prototypes. We employ a surface-patterning technique enabling both the selection of a target higher-order mode and a reshaping of its FF profile, by etching a grating-relief array in the VCSEL cap layer and growing a dielectric rephasing section. After having identified the rectangle and the donut as optimal oxide aperture shapes in terms of thermal dissipation and FF properties, corresponding prototypes are experimentally fabricated and measured, confirming the simulations. For the rectangle, a SPM power of 13 mW is demonstrated; for the donut, a doubled maximum SPM power of 27 mW, both with centered FFs. The presented results pave the way for continuous-wave high-power single-mode axial-emitting VCSELs, exceeding the previously reported SPM power values. 100 mW are then predicted, grounded on the above achievements. This is particularly interesting for quantum sensing and free-space communication and will certainly attract interest in other applications that have not yet addressed VCSELs due to their current too-low SPM power performance.**

***Index Terms*—VCSEL, large aperture, single-mode, high-power, axial far-field, quantum sensing, surface patterning.**

I. Introduction

VERTICAL-CAVITY surface-emitting lasers (VCSELs) are a cornerstone of compact photonics for low-power applications, as they combine wafer-scale manufacturability, low threshold current, surface emission, and high efficiency. In short-range datacenter communications, III-V VCSELs with circular output beams enable high modulation bandwidth transmitters for optical interconnects [1], [2], [3]. In this context, devices typically deliver 2 to 6 mW of optical power and operate either in single-mode (SM) or few-mode regime depending on the optical link requirements [4], [5], [6]. In datacom, the modulation bandwidth is the dominant design constraint, leading to small modal volumes [7]. As a consequence, datacom VCSELs are intentionally designed with aperture diameters close to 4 μm, inherently restricting the maximum extractable optical power while enabling high-speed operation.

Emerging applications such as chip-scale atomic clocks, magnetometers and quantum gyroscopes impose substantially different requirements. In these systems, VCSELs operate as atomic pump sources exciting well-defined alkali transitions [8], [9]. The emission wavelength must precisely match atomic lines, e.g., Cs at 894.6 nm and Rb at 794.8 nm, and the source must provide single-mode, single polarisation (SPM altogether), narrow linewidth, and continuous wave (CW) emission. Increasing the available SPM optical power is highly desirable, as it enables more efficient atomic pumping and enhances the robustness of compact quantum sensors [10]. Axial far-field (FF) emission further represents a significant advantage in compact free-space applications, where multi-lobed or off-axis FF profiles require bulky external optics to reshape or recombine the multiple beams, thereby compromising system integration [11].

A representative application is within the QYRO project [9], focusing on the first satellite-based quantum gyroscope in 2027, for which the atomic pump VCSELs analysed in this work have been specifically developed. In this framework, the pump device must deliver at least 10 mW SPM output power at the Rb transition around 795 nm in CW regime at 30 °C of heat-sink temperature, together with single-polarisation, precise spectral control and a linewidth lower than 100 MHz.

Power scaling in oxide-confined VCSELs can be achieved by increasing the active area [12] and/or enhancing the internal quantum efficiency by cascading more active regions [13], [14]. However, both solutions lead to higher self-heating, resulting in earlier thermal rollover in CW operation. This limitation is particularly severe in circular oxide apertures.

Received 25 March 2026; revised 27 May 2026; accepted 29 June 2026. Date of publication 3 July 2026; date of current version 23 July 2026. This work was supported by QYRO Project through the German Federal Ministry of Research, Technology and Space under Grant Agreement 13N16314 (TRUMPF Photonic Components). *(Corresponding author: Matteo C. G. Alasio.)*

Valerio Torrelli, Martino D'Alessandro, Francesco Bertazzi, Michele Goano, and Matteo C. G. Alasio are with the Department of Electronics and Telecommunications (DET), Politecnico di Torino, 10129 Torino, Italy, and also with Istituto di Elettronica e di Ingegneria dell'Informazione e delle Telecomunicazioni (IEIIT) del Consiglio Nazionale delle Ricerche (CNR), 10129 Torino, Italy (e-mail: matteo.alasio@polito.it).

Alberto Gullino and Pierluigi Debernardi are with Istituto di Elettronica e di Ingegneria dell'Informazione e delle Telecomunicazioni (IEIIT) del Consiglio Nazionale delle Ricerche (CNR), 10129 Torino, Italy.

Julian Lindner, Stephan Gronenborn, Markus Herper, Tobias Pusch, and Holger Moench are with TRUMPF Photonic Components GmbH, 89081 Ulm, Germany.

Gabriele Moiso and Alberto Tibaldi are with the Department of Electronics and Telecommunications (DET), Politecnico di Torino, 10129 Torino, Italy.

Color versions of one or more figures in this article are available at https://doi.org/10.1109/JSTQE.2026.3710026.

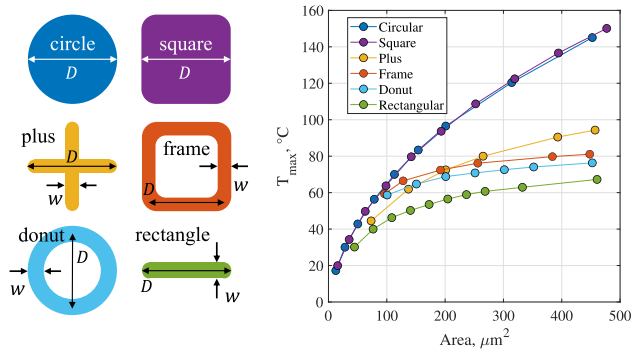
Digital Object Identifier 10.1109/JSTQE.2026.3710026

© 2026 The Authors. This work is licensed under a Creative Commons Attribution 4.0 License. For more information, see https://creativecommons.org/licenses/by/4.0/

TABLE I
SUMMARY OF THE MEASURED FIGURES OF MERIT FOR THE RECTANGULAR AND DONUT SHAPED OXIDE APERTURE VCSELS UNDER ANALYSIS. THE ROLLOVER POINT IS CHOSEN AS THE GLOBAL MAXIMUM OF THE OPTICAL POWER.

Oxide shape	Rephasing	Area μm^2	Max. SPM power mW	Max. SPM dens. $mW/\mu m^2$	SPM range mA	P_{diss} (rollover) mW	P_{diss} dens. (rollover) $mW/\mu m^2$	I_{th} mA	SE W/A	WPE %	R_d Ω	R_{th} °C/mW
Circle (Ref.)	No	15.9	4.6	0.29	I_{th}–rollover	16	1.03	0.80	1.01	33.4	165	3.22
Rectangle	No	107	15	0.14	8–22	46	0.43	2.9	0.96	31.7	48	1.14
Rectangle	Yes	107	13	0.12	I_{th}–18	38	0.36	3.1	1.00	33.1	47	0.96
Donut	No	330	33	0.10	I_{th}–rollover	100	0.30	8.7	1.00	31.5	19	0.49
Donut	Yes	330	27	0.08	I_{th}–rollover	99	0.30	11.1	0.84	25.0	18	0.49

In this paper, we discuss the optimal active shape through comprehensive investigations of the thermal and optical problems (in order of relevance) using our in-house VCSEL ELectro-Magnetic Suite (VELMS) [15], [16]. In fact, temperature rules VCSEL operation in all senses, while the optical aspect can be handled and engineered more comfortably. To this end, we first investigate how the heat source shape, related to the oxide aperture [17], [18], [19], [20], affects the corresponding self-heating temperature profile. Then, we perform a similar study on the related FF features, seeking a good balance between FF pattern and heat dissipation. In fact, we aim for centred far-fields for apertures whose beam waists are comparable to those of standard circular VCSELs. We identify the two best candidates as the rectangular and the donut-shaped apertures. For both, we optimise their surface-patterning designs and experimentally verify their performance. We achieve record SPM output powers for both geometries, with axial emission. Building on these results, we propose a design aimed at higher output powers. We predict more than 100 mW SPM output power with axial FF emission by simulating a larger donut VCSEL with improved threshold gain, dichroism, transverse mode control and similar maximum inner temperature as in the manufactured VCSELs. Our work builds on the experimental results reported in [21], which however focuses only on the rectangular shape. Here, on the other hand, we aim to give a comprehensive thermal and electromagnetic background for many VCSEL shapes, demonstrating both theoretically and experimentally that a donut-shaped VCSEL allows for improved single-mode stability and axial emission.



(a) Sketch of the investigated oxide aperture shapes.

(b) Maximum temperature variation with respect to the heat sink at the VCSEL substrate as a function of the oxide aperture area.

Fig. 1. Analysis of the temperature variation at equal dissipated power density of 0.30 $mW/\mu m^2$, for different oxide aperture shapes and dimensions D, keeping fixed $w = 4\,\mu m$.

II. OXIDE APERTURE OPTIMISATION

This is a simulative section, where we provide the guidelines for an optimal design. It is based on our 795 nm epitaxial structure, whose main features are provided below. It will be used for both the thermal and optical analysis of the following sections.

A. Oxide Aperture Impact on Thermal Performance

The oxide aperture geometry is the result of a trade-off between efficient thermal dissipation and SPM operation. In Fig. 1(a), the investigated oxide shapes are sketched: circle, square, rectangle, plus, frame and donut, with dimensions w and D.

To assess self-heating in these geometries, we compute and compare the self-heating temperature under equal dissipated power density (P_{diss} per unit area). For a rigorous treatment, the microscopic thermal sources related to Joule heating, free-carrier absorption and non-radiative recombination should be computed within the whole VCSEL [22]. In this work, we adopt analytic fitted expressions of the actual heat sources [20], which allow us to perform thermal simulations using an in-house 3D finite element thermal solver ([18], using the same thermal conductivities). A dissipated power density of 0.30 $mW/\mu W^2$ (corresponding to the experimental value at rollover for donut VCSELs listed in Table I), a substrate thickness of 150 μm (corresponding to the manufactured structures) and $w = 4\,\mu m$ are kept fixed, while the aperture area changes by acting on D. The resulting maximum self-heating temperature rise with respect to the heat sink temperature is shown in Fig. 1(b). The rectangular and donut oxide aperture shapes provide the most efficient thermal dissipation, while the non-elongated compact geometries (circle and square) perform the worst. This explains why square geometries used in previous axial FF single-higher-order-mode devices exhibited early rollover and limited output power of 3 mW [23]. Elongated oxide apertures improve thermal management, since the reduced dimension along the short axis enhances lateral heat dissipation and mitigates self-heating temperature rise [12], [19]. Nevertheless, increasing the active area for both compact and elongated geometries naturally promotes higher-order transverse modes and therefore multi-mode emission [24], [25], [26].

B. Oxide Aperture Impact on FF Performance

Following the thermal analysis, we estimate the properties of the FF profile associated with the considered oxide shapes. As a starting point, we compute the FF of the corresponding fundamental modes, by means of our electromagnetic solver VELMS. The circle and the square are not included, due to their poor

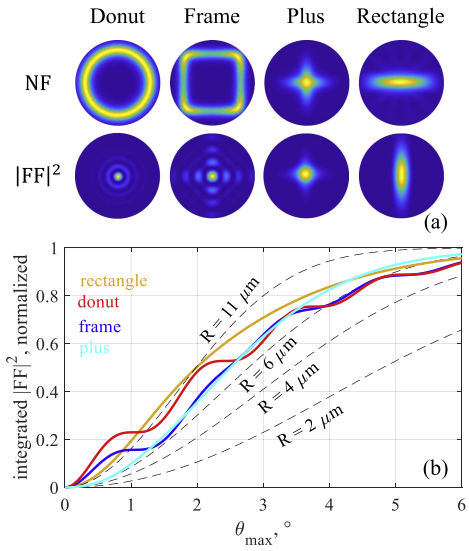


Fig. 2. Simulated NF and FF intensity profiles of the fundamental mode for the investigated oxide aperture shapes at 50 °C, with $w = 4\,\mu$m and $D = 36\,\mu$m. (a) NF and FF for the shapes sketched in Fig. 1(a), excluding circle and square for their inefficient thermal management. All fields are normalized between 0 (blue) and 1 (yellow). (b) $\mathcal{I}(\theta_{\max})$ for the investigated shapes (solid lines, see legend), compared to those of the fundamental mode of a circular aperture with increasing D (dashed lines).

thermal performance [23], [24]. In fact, the fundamental mode represents the narrowest on-axis ideal FF for a given aperture. However, such modes cannot be exploited in the large-aperture devices, required for power scaling.

Preserving SPM operation at enlarged apertures requires engineered modal discrimination. This was demonstrated by selecting a higher-order mode via surface patterning of the top mirror, creating a reflectivity profile tailored to the targeted higher-order mode [27]. When polarisation control is of concern, monolithically integrated subwavelength grating reliefs (GR) can be etched instead [27], [28], [29], [30]. By designing a reflectivity profile that matches that of the desired transverse mode, one promotes that mode over its opponents, by making its threshold gain G_{th} the lowest [31]. In the case of GR arrays acting on each peak of a certain higher-order mode the resulting FF is off-axis [27] (just like the one in Fig. 5(b). We will address this issue in more detail later. Here, briefly, we anticipate that one can rephase all the negative parts of the mode to recover in-phase emission. This mimics the emission features of a fundamental mode. By definition, its emission is in phase everywhere at the output, so that its FF is on-axis, as shown in Fig. 2(a).

In Fig. 2(b), we report the intensity squared-magnitude FF integrated over a circular angular region vs. the integration angle $\theta_{\max}$, namely:

$$\mathcal{I}(\theta_{\max}) = \frac{\iint_{\{\alpha^2+\beta^2\le\theta_{\max}^2\}} |\text{FF}(\alpha,\beta)|^2 \,\text{d}\alpha\text{d}\beta}{\iint_{\mathbb{R}^2} |\text{FF}(\alpha,\beta)|^2 \,\text{d}\alpha\text{d}\beta}, \qquad (1)$$

where (α, β) represent the FF cartesian angular coordinates. The considered geometries fall into two distinct families, which we refer to as *annular* and *connected*. Connected geometries, such as the rectangle and the plus, exhibit a smooth FF behavior similar to standard circular VCSELs (see black dashed lines). Annular geometries, like the donut and the frame, always exhibit ripples in the FF.

Among the connected geometries, the rectangular aperture provides the best overall behavior, both thermally and optically. In particular, it dissipates heat more efficiently than the plus, which suffers from a stronger current crowding effect at centre. Additionally, the sharp angles associated to the intersections of the plus-shaped oxide aperture represent disturbances for the targeted optical field, possibly producing cross-talk between lobes of the selected higher-order mode, making the surface-patterning design trickier.

From the FF standpoint, the rectangular aperture suffers of two main drawbacks. One is the elongated FF along its short axis. The second, even worse, is related to self-heating at high injection currents. In fact, thermal lensing modifies the effective refractive index [32], [33], squeezing the mode to the centre of the long axis [19]. This eventually breaks single-mode operation. By contrast, annular geometries are not prone to this effect, since thermal lensing acts radially, where the mode is constrained by the aperture shape, but the modal alignment with the surface patterning depends on the azimuthal distribution, which remains unaltered. The improved single-mode stability for annular geometries is achieved at the cost of a FF profile with ripples, highlighting a trade-off which depends on the specific application. This will be further addressed when commenting the experimental results.

III. Design and Results

In this section, we present an optical analysis providing design rules to achieve SPM operation in the shapes of choice previously discussed, namely the rectangle and the donut. We aim to obtain a rephased output-field modal pattern for central FF emission, extending the results presented in [27].

The structure under analysis is based on an electrically pumped oxide-confined *pin* AlGaAs VCSEL emitting at $\lambda = 795$ nm, grown on a GaAs (100)-substrate. The epitaxial structure comprises a 1λ optical cavity with three AlGaAs quantum wells (QWs) with low Al-content (photoluminescence peak at 783 nm), sandwiched between two graded distributed Bragg reflectors (DBRs) to improve electrical performance. The bottom Si-doped n-DBR comprises 41 mirror pairs, while the top C-doped p-DBR consists of 21 pairs, enabling top-side emission.

The uppermost GaAs layer of the top DBR, referred to as the phase matching layer (PML), provides a low-resistance path to the Ti/Pt/Au p-contact. As well known, the reflectivity of the top DBR exhibits a periodic dependence on the PML thickness t_{PML}, with period $\lambda/(2\,n_{\text{PML}})$, where $n_{\text{PML}} = 3.6$ is the refractive index of GaAs at 795 nm. An in-phase PML condition corresponds to a maximum DBR reflectivity, while a thickness variation of $\lambda/(4\,n_{\text{PML}})$ leads to an out-of-phase condition, with minimum reflectivity.

For the fabricated VCSELs, a 100 nm-thick out-of-phase PML is considered. Modal selectivity is enforced through surface patterning of this layer. Specifically, regions corresponding to the transverse intensity lobes of the targeted mode are locally etched, thereby restoring the in-phase condition and increasing the mirror reflectivity. This spatial modulation of reflectivity

reduces the threshold gain G_{th} of the selected transverse mode relative to the others.

To achieve both modal and polarisation discrimination, the surface patterning is implemented using subwavelength GRs featuring a period of $\Lambda = 143$ nm and a duty cycle (DC) of 38%. A 75 nm-deep etch leaves 25 nm of residual GaAs beneath the etched regions, with 55 nm wide GaAs bars in air, oriented along [0-11]. In our optical solver, the GR is treated through a homogenization procedure [16], [27], [34], [35]. The patterned region is modelled as an effective anisotropic medium characterised by transverse electric (TE) and transverse magnetic (TM) effective refractive indices, which were found to be $n_{\text{TE}} = 2.53 - 0.04j$ and $n_{\text{TM}} = 1.66 - 0.01j$. The corresponding longitudinal TM refractive index profile $n(z)$ (black curve) and normalised standing wave (red curve, logarithmic scale) are shown in Fig. 3. For the chosen parameters, the reflectivity associated with the TM effective index exceeds that of the TE polarisation, leading to G_{th} of the targeted mode of 1955 and 2225 cm^{-1}, respectively. The GR therefore provides simultaneous transverse-mode selection and polarisation control through engineered mirror reflectivity.

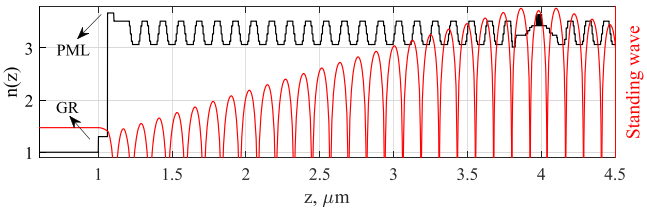


Fig. 3. Longitudinal refractive index $n(z)$ (black) and electromagnetic standing wave in logarithmic scale (red), normalized to its maximum value, for the VCSEL design under analysis.

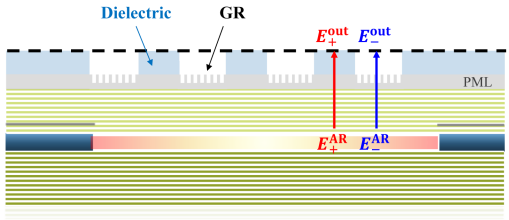


Fig. 4. Schematic cross-sectional view of a large-area rectangular VCSEL illustrating the GRs and the dielectric rephasing elements. A qualitative representation of the optical field propagation from the active region to the top of the dielectric is also shown, highlighting two adjacent lobes with a relative phase difference of π. The field evolution is depicted both beneath the GRs and the dielectric elements.

A. *Rephasing Dielectric Elements*

After selecting the target mode through GR-based surface patterning, the chosen higher-order transverse mode exhibits a multi-lobed near-field (NF) with alternated signs, as shown in [27], which evolves in free-space into an off-axis FF [21].

To restore axial FF emission, an additional manufacturing step is required, by introducing a rephasing dielectric [36] patterned layer on top of the VCSEL, as sketched in Fig. 4. The rephasing elements are fabricated in silicon nitride, with refractive index $n_{\text{diel}} = 2$, and positioned according to the NF topography of the selected mode. Their role is to locally modify the optical phase of specific lobes, compensating the intrinsic π phase difference between adjacent intensity maxima. Therefore, we introduce a dielectric rephasing element every two NF lobes. In principle, the dielectric could be grown directly on top of the gratings, positioned at each intensity lobe. However, silicon nitride deposition on a grating may introduce unpredictable geometries, such as partial trench filling between the grating bars. To avoid possible problems, we adopt an alternating scheme: instead of placing a GR at every lobe, GRs are etched only every second NF lobe. The dielectric rephasing elements are thus grown on the complementary sites, directly on the flat facet without gratings. These elements are laterally extended node-to-node of the targeted transverse mode. This alternating GR–dielectric arrangement, schematically illustrated in Fig. 4 [27], enables controlled rephasing while preserving structural flatness and technological reliability.

Two design requirements must be simultaneously satisfied when introducing the rephasing elements. First, the top DBR in the rephasing section after the silicon nitride deposition must be in-phase and with maximum reflectivity. A similar phase-engineering principle used for the GR is adopted here. Starting from an out-of-phase cap layer, the addition of a dielectric thickness of at least $\lambda/(4n_{\text{diel}})$ is required to restore an in-phase optical condition. Any $\lambda/(2n_{\text{diel}})$ addition equally ensures that the dielectric region operates at high reflectivity. Second, the optical fields originating from the active region (AR) beneath the GR and beneath the dielectric region must have the same phase at the output plane. The optical field at the AR exhibits alternating signs; as schematized in Fig. 4, we denote as E_+^{AR} the field lobes located below the etched GR regions and E_-^{AR} those located below the dielectric elements. Using a transmission-matrix formalism for normal-incidence [16], the field E_+^{AR} is propagated up to the output plane through the DBR and GR stack, while E_-^{AR} is propagated to the same longitudinal coordinate including an air layer having the same thickness as the dielectric layer. The objective is to minimize the phase difference at the output plane, defined as $\Delta\phi = \angle E_+^{\text{out}} - \angle E_-^{\text{out}}$, thereby enforcing constructive interference, resulting in a centred FF emission. The optimal dielctric thickness t_{diel} is therefore determined by simultaneously maximising reflectivity and minimising $\Delta\phi$.

We highlight the impact of the dielectric layer in Fig. 5, showing different quantities as functions of t_{diel}. The structure includes both GRs and dielectric elements, aiming at selecting the mode with five lobes along the long side and one lobe along the short side [27]. In Fig. 5(i), the top DBR reflectivity evaluated with the transmission matrix formalism shows that the starting point ($t_{\text{diel}} = 0$) is close to a minimum due to an out-of-phase PML; a $\lambda/(4n_{\text{diel}})$ increment brings the reflectivity to a maximum; every subsequent $\lambda/(2n_{\text{diel}})$ variation preserves the reflectivity maximum. Fig. 5(ii) reports the G_{th}/QW (threshold gain per quantum well, namely the gain that each QW must provide to compensate all the losses) of the selected mode from fully 3D VELMS simulations, with an opposite behavior to the reflectivity profile: a high reflectivity is related to low G_{th} and viceversa. Fig. 5(iii) shows $\Delta\phi$, which is periodic with period $\lambda/(n_{\text{diel}} - n_{\text{air}})$, significantly longer than $\lambda/(2n_{\text{diel}})$ of the reflectivity.

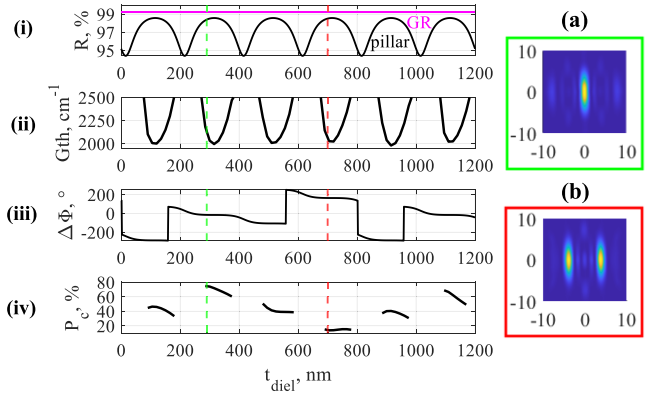


Fig. 5. Dependence of the considered design parameters on the dielectric thickness. Reflectivity of the top DBR at the dielectric section (black curve) and at the GR section (magenta curve) (i), threshold gain from 3D VELMS simulations (ii), phase difference at the output plane (iii) and central power from VELMS (iv) as functions of t_{diel}. The corresponding FFs at $t_{\text{diel}} = 290$ nm (green) and 700 nm (red) are reported in the insets (a) and (b), respectively. The axes are in degrees and the field is normalized between 0 (blue) and 1 (yellow).

By combining the information extracted from these results, we identify that a suitable dielectric thickness corresponds to the second reflectivity maximum, approximately $t_{\text{diel}} = 290$ nm, where $\Delta\phi$ is also minimal (see green dashed line in Fig. 5), which makes the output field lobes interfering constructively. This is also confirmed by the fields reported in Fig. 5(a)–(b), where the FF from VELMS features an axial pattern for $t_{\text{diel}} = 290$ nm (green box) and is off-axis for $t_{\text{diel}} = 700$ nm (red box). From them, we can estimate the fraction of axial power as a function of t_{diel}, by defining the central power P_c as the integral of the FF intensity distribution between $-3°$ and $+3°$ along the long side of the aperture, normalized by the total intensity. We observe that P_c reported in Fig. 5(iv) follows the same trend as $\Delta\phi$, with maxima corresponding to $\Delta\phi$ zeros. The missing values correspond to non-lasing regions of t_{diel} intervals, because of their too high G_{th}. Also VELMS simulations confirm that the FF pattern periodicity with t_{diel} is the same as that of $\Delta\phi$, namely $\lambda/(n_{\text{diel}} - n_{\text{air}})$.

We establish explicit design rules that simultaneously optimise threshold performance and axial FF, extending [27]. In particular, we demonstrate that the optimal dielectric thickness can be determined through straightforward one-dimensional simulations under normal incidence, based on the transmission-matrix formalism. Such one-dimensional transmission-matrix tools are widely available and implemented in most commercial optical simulation packages, making the proposed design procedure both accessible and easily reproducible.

B. Experimental Setups

Concerning the experimental characterization, we measured the light-intensity-voltage (*LIV*) characteristics, optical spectra, FF, orthogonal polarisation suppression ratio (OPSR, [29]) and polarisation-resolved near-field. For *LIV*s and spectra, the full wafer was placed on a temperature-controlled chuck, ensuring a constant backside temperature during operation. The laser devices were electrically driven with a Keithley 2612 source-measure unit and the laser output was coupled into a calibrated integrating sphere for optical power measurements. The OPSR can be simply measured by adding a linear polariser. An additional fiber port equipped with an SMA-terminated multimode fiber enabled simultaneous spectral acquisition using an Ocean Optics HR4000 spectrometer with an optical resolution of 0.1 nm. For FF measurements, all devices were mounted on dedicated measurement boards and attached to a copper heat sink using a thermally conductive adhesive. The FF distribution was measured with a Cinogy Cincam 1.001 nano camera, where the divergent beam was propagated onto the sensor at a distance of 10mm. Finally, polarisation-sensitive near-field images were recorded using an Instrument Systems VTC4000 camera, confirming single-polarisation behavior with a measured polarisation contrast of $> 95\%$ (limited by the camera's resolution).

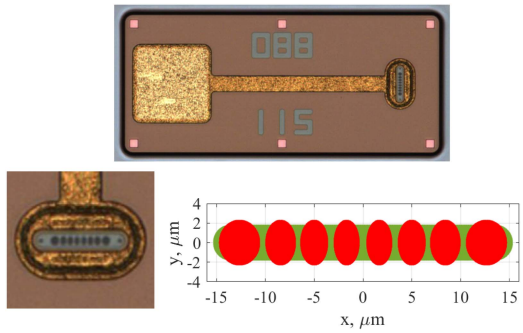


Fig. 6. Top view of the whole VCSEL chip. Bottom left: magnification on the rectangular VCSEL, with GRs and no dielectrics. The metal p-contact is formed by the two horizontal stripes above and below the GR array. Bottom right: a magnified schematic of the GR array (in red) and rectangular oxide aperture (in green). The dimensions of the rectangle are $30.5 \times 3.5\,\mu\text{m}^2$.

C. Rectangular Oxide Aperture

For both structures, rectangle and donut, a target width of $w = 4\,\mu$m was defined. The fabricated devices exhibit a measured width of approximately $w = 3.5\,\mu$m, which is remarkably close to the design target considering the intrinsic tolerances of the oxidation process [37]. In contrast, the dielectric thickness was accurately realized at $t_{\text{diel}} = 290$ nm, as designed in Section III-A.

We defined a rectangular oxide aperture with rounded corners of $30.5 \times 3.5\,\mu\text{m}^2$, whose chip is depicted in Fig. 6. Its cap layer incorporates the GR array highlighted in red in the same figure, designed to select the transverse mode featuring eight intensity peaks along the long side and a single peak along the short side [9], [16], [27].

The corresponding experimental and simulated results are reported in Fig. 7. As shown in Fig. 7(a), the CW *LI* curve exhibits a first change in slope at approximately 8 mA, suggesting that the device does not initially lase in the targeted 8-peak mode. A second slope variation occurs at 22 mA, marking the onset of multi-mode operation and limiting the maximum SPM output power to 15 mW. The transitions are attributed to thermal lensing, which compresses all modes toward the center of the aperture, first aligning and then, eventually, misaligning the 8-peak mode with the etched GR regions. The threshold

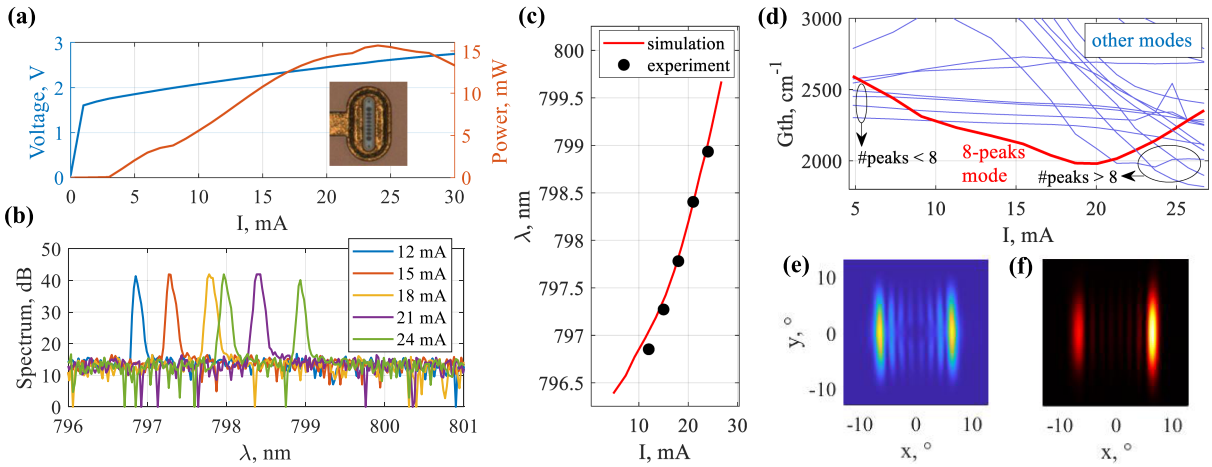


Fig. 7. Experimental data and simulation results at heat sink temperature of 30 °C for the rectangular aperture VCSEL with GRs. (a) Measured *LIV* curves, showcasing a maximum SPM power of 15 mW at around 22 mA. The inset reports the top view of the chip. (b) Measured optical spectra at different injection currents. Multi-mode transition occurs between 21 and 24 mA. (c) Wavelength red-shift of the selected mode, reproduced by VELMS simulations. (d) Threshold gain G_{th} vs current, from VELMS. (e)–(f) Simulated and measured (at 14 mA) non-axial FF pattern, respectively.

current is $I_{\text{th}} = 2.9$ mA, with differential resistance $R_{\text{d}} = 48\,\Omega$, maximum wall-plug efficiency (WPE) of 31.7% at 16 mA, and slope efficiency (SE) of 0.96W/A. The measured emission spectra at room temperature for increasing injection currents are reported in Fig. 7(b), confirming the transition to multi-mode emission between 21 mA and 24 mA. The wavelength red-shift of the 8-peak mode as a function of current is shown as black circles in Fig. 7(c), exhibiting excellent agreement with the simulated curve (red line). The simulations are performed assuming $dn/dT = 3 \times 10^{-4}\text{K}^{-1}$ [32], [38] and adopting the thermal conductivity values reported in [20, Table I]. Fig. 7(d) reports the simulated G_{th} of all the identified transverse modes as a function of the injection current I. The results confirm that below 10 mA and above 20 mA the 8-peak mode experiences a strong modal competition. At higher currents, the 9-peak mode becomes dominant, in agreement with the theoretical predictions of [19]. Although the device provides a relatively wide SPM range in the targeted mode, these results show that the surface-patterned design is bias-dependent, as discussed earlier. Without rephasing, the FF shown in Fig. 7(e)–(f) exhibit a non-axial profile, with two dominant lobes at large angular distance, fully consistent with the theoretical expectations.

By applying the design rules discussed in Section III-A, we retrieve axial emission, as shown in Fig. 8(c)–(d). From the manufacturing standpoint, the rephasing elements are realised by a silicon nitride layer with the designed thickness of $t_{\text{diel}} = 290$ nm, deposited on top of the cap layer. This was subsequently patterned by selective openings at the GR regions (the blue areas in Fig. 10). As a result, the optical field effectively experiences an alternating sequence of GRs and dielectric elements, as intended.

For the rephased sample, the *LIV* curves in Fig. 8(a) show that the SPM emission is lost at around 18 mA, and the threshold current slightly increases to 3.1 mA. We demonstrate a maximum axial SPM output power of 13 mW at 18 mA, with an elongated axial FF along the short side of the rectangular aperture. This is very similar to that of the fundamental mode FF pattern reported in Fig. 2(a), therefore validating our approach. We find a peak

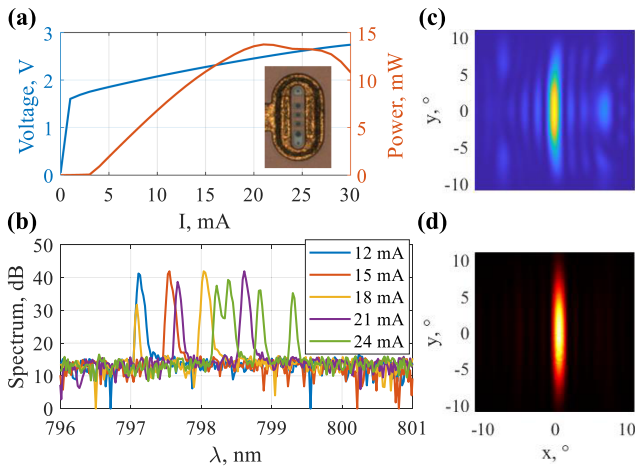


Fig. 8. Impact of optimised rephasing design on the rectangular aperture VCSEL at 30 °C. (a) Measured *LIV* characteristics: SPM mode emission is lost at around 18 mA, with a maximum SPM power of 13 mW. The inset reports the top view of the chip. (b) Wavelength spectra at increasing bias current. (c)–(d) Simulated and measured (at 18 mA) FF patterns, respectively.

WPE of 33.1%, with SE $= 1.00\,\text{W/A}$. The rephasing layer primarily affects the selected mode FF pattern, as we desire, leaving the other CW figures of merit almost unchanged. The emission spectra at increasing bias current (Fig. 8(b)) show that at 18 mA the spectrum features two peaks, with the shorter wavelength one (related to a higher-order mode) more than −10 dB below the selected mode peak at 798 nm. Such a secondary peak becomes relevant at 21 mA, after rollover. Together with [21], these results show the feasibility of CW, SPM high-power, axial-emitting VCSEL operation over the full useful operating range, supporting the proposed design.

D. Donut Oxide Aperture

In the rectangular design, the axial FF has an oblong shape along the short side of the aperture. In addition, a non-intended higher-order mode appeared before the VCSEL turn-off. In

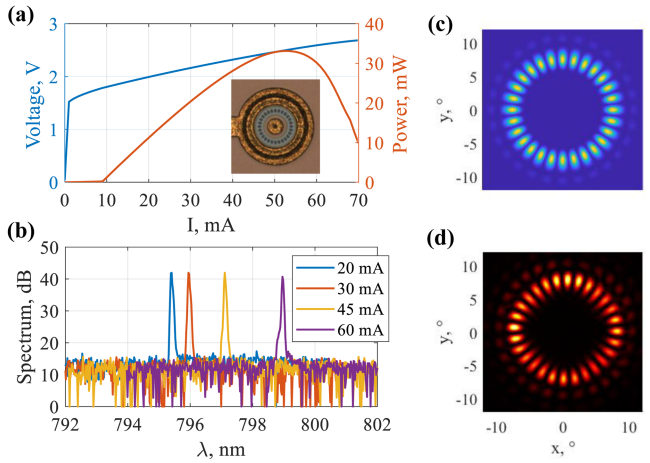


Fig. 9. Experimental E results on the donut-shaped aperture VCSEL at 30 °C, with GR and without rephasing elements. (a) Measured CW *LIV* characteristics: the SPM emission is maintained for the whole bias window, with a maximum SPM power of 33 mW at 53 mA. The inset reports the top view of the chip. (b) Wavelength spectra at increasing bias current. (c)–(d) Simulated and measured (at 42 mA) FF patterns, respectively.

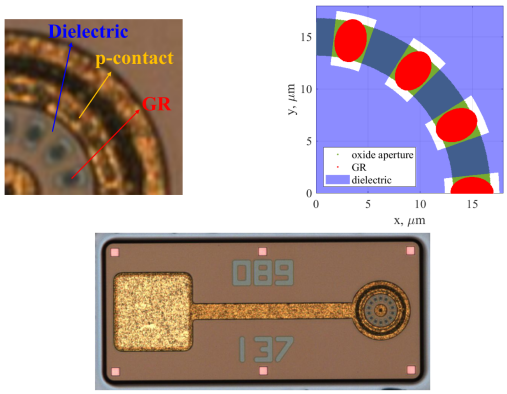


Fig. 10. Top view of the VCSEL chip. Top left: magnification on the donut shaped VCSEL, with a GR array and a dielectric rephasing layer. The metal p-contact is the ring outside the aperture. Top right: a one-quarter schematic of the GR array (in red), the dielectric rephasing layer (in blue) and a donut oxide aperture (in green), with $D = 30\,\mu$m and $w = 3.5\,\mu$m. In the schematic the metal contact layers are not included.

Fig. 9, we report the performance of the donut-shaped oxide aperture VCSEL. Our results demonstrate its ability to overcome both issues, providing a direct comparison with the rectangular design. Both structures were based on the same epitaxial structure.

First, we consider a donut with $w = 3.5\,\mu$m and $D = 30\,\mu$m, with 28 GRs, selecting the whispering-gallery mode [39], [40] with 28 azimuthal peaks, and no rephasing elements. Compared to the rectangle, a major advantage of this geometry is that the self-heating profile induces a radial thermal lensing, whereas the alignment of the selected mode with the reliefs depends only on the azimuthal positions. As a result, the radial thermal lensing does not affect the field alignment as the bias current increases. This leads to a robust SPM operation throughout the entire operating range, as demonstrated by Fig. 9(a). The *LI* curve does not show any slope change, and the threshold current is 8.7 mA. The SPM maximum output power of 33 mW is

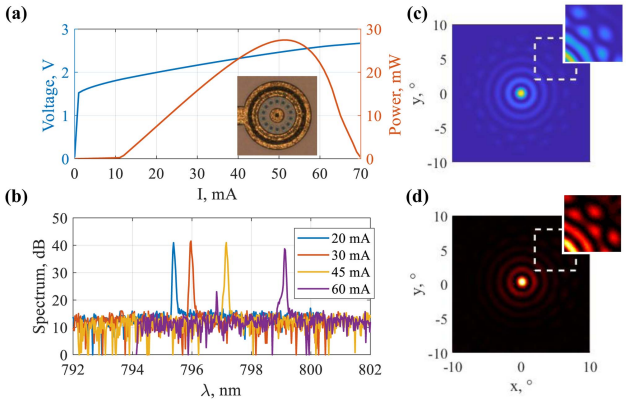


Fig. 11. Impact of the dielectric design on the donut aperture VCSEL, at 30 °C. (a) Measured CW *LIV:* the SPM emission is maintained for the whole bias window, with a maximum SPM power of 27 mW. The inset reports the top view of the chip. (b) Wavelength spectra at increasing current. (c) Simulated FF pattern and (d) corresponding measured FF at 42 mA.

reached at 53 mA. This value, obtained for *pin* VCSELs without multi-junctions [41], is approximately four times higher than the previously reported result [42], despite the more demanding 795 nm wavelength range. Indeed, operation at 795 nm requires a higher Al-content compared to standard 850 nm VCSELs, including in the quantum wells, which generally leads to a degradation of the overall device performance.

The WPE is 31.5% at 31 mA, with SE $= 1.00\,\mathrm{W/A}$. The differential resistance of 19 Ω more than halves with respect to the rectangular design and the emission remains in the SPM regime for the whole operation window, as shown by the spectra reported in Fig. 9(b). Without the rephasing elements, the measured FF in Fig. 9(d) remains non-axial, with excellent agreement with the simulated pattern reported in Fig. 9(c).

To retrieve axial emission, we apply the same GR-dielectric design pattern as before, as depicted in Fig. 10, implying that now only 14 GRs are present in the structure, with silicon nitride between them. The impact of the dielectric layer is comparable to the rectangular case and is reported in Fig. 11. The *LI* in Fig. 11(a) displays a record peak SPM axial output power of 27 mW at 51 mA, with an oxide aperture area of $330\,\mu\mathrm{m}^2$ and an SPM power density of 0.08 mW/μW^2, significantly reduced from the rectangular aperture case. The introduction of the rephasing dielectric section leads to an increase of the threshold, leading to $I_{\mathrm{th}} = 11.1$ mA, and a corresponding lower SE $= 0.84\,\mathrm{W/A}$ and WPE $= 25.0\%$. The increase of I_{th} when introducing the rephasing can be explained by means of Fig. 5(b)(i). Even when the rephasing element is optimised for the best possible reflectivity, the reflectivity at the dielectric section still remains lower than that at the GR section. Our designed rephasing pattern places a GR every second peak, thereby decreasing the overall modal DBR reflectivity. The measured on-axis FF pattern in Fig. 11(d) is well reproduced by the simulated FF in Fig. 11(c). It features circular symmetry, which is very similar to that of the ideal fundamental donut mode FF of Fig. 2(a), proving again the simplified approach of Section II. As already discussed in the design without rephasing

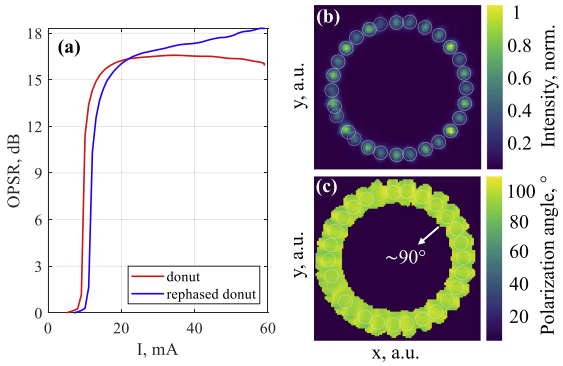


Fig. 12. (a) Measured OPSR as a function of current for the donut structures, with and without the rephasing layer. (b) Measured near-field distribution and (c) linear polarisation angle ($\sim 90°$, aligned with the y axis) for the rephased donut at 30 mA. White circles indicate the peak positions automatically detected by the camera.

pattern, the wavelength spectra never show an additional peak, even at rollover current.

Concerning the polarisation performance, the OPSR of the rectangle, both with and without the rephasing layer, is reported in [21]. For the donut, Fig. 12(a) shows a good OPSR for both regular and rephased VCSEL structures. Fig. 12(b) shows the near-field profile of the latter, while Fig. 12(c) shows the linear polarisation angle distribution over the transverse plane. The grating bars are aligned with the x axis of the reference system of the images, thus a polarisation angle of 90° confirms the TM-polarisation emission.

For all VCSELs presented so far, we measured their linewidth using the delayed self-homodyne method [43], resulting in a range of 5 to 15 MHz, which is compatible for atomic pumping applications [9]. The overall CW figures of merit for the investigated devices are summarised in Table I.

As a reference, in the first row of Table I we also show the properties of a circular VCSEL with an oxide aperture diameter 4.5 μm and circular GR of diameter 3.5 μm, processed from the same wafer as the other investigated devices.

E. Extraction of Thermal Resistance

As a final remark, we estimate the thermal resistance R_{th}, defined as the ratio between the VCSEL temperature increase to the corresponding dissipated power. To this end, we estimated $d\lambda/dT \approx 0.07$ nm/°C, in agreement with [44], by measuring the wavelength shift between 30 °C and 60 °C of heat-sink temperature, close to threshold where self-heating is negligible. The corresponding *LIV* characteristics at 60 °C worsen since cavity detuning was optimized for 30 °C according to the requirements of the Qyro project [9]. The emission wavelength is then plotted as a function of the dissipated power in Fig. 13(a), revealing a linear dependence with slope $d\lambda/dP_{\text{diss}}$. Since wavelength, dissipated power, and temperature are all linearly related to one another, the thermal resistance can be experimentally estimated as [44]:

$$R_{\text{th}} = \frac{d\lambda}{dP_{\text{diss}}} \left(\frac{d\lambda}{dT} \right)^{-1}. \tag{2}$$

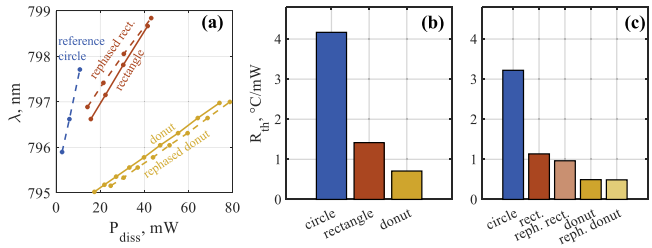


Fig. 13. Thermal resistance analysis. (a) Measured λ vs. P_{diss} for the investigated devices at heat-sink temperature of 30 °C. (b)–(c) Simulated and measured R_{th}, respectively.

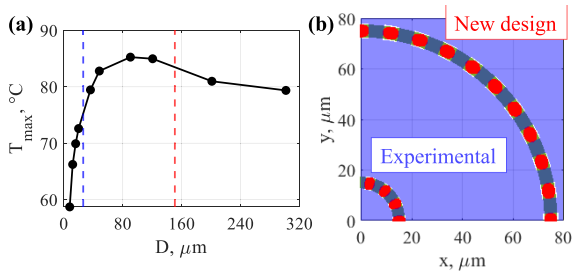


Fig. 14. (a) Simulated maximum inner temperature in donut aperture VCSELs at a fixed dissipated power density of 0.30 mW/μm^2, saturating at increasing diameters ($w = 4\,\mu$m). Blue and red dashed vertical lines denote two analyzed designs. (b) Sketch of donut apertures patterning in the first quadrant.

From the simulation side, R_{th} can instead be directly extracted from Fig. 1 from the ratio between the simulated temperature increase and dissipated power. The final comparison is reported in Fig. 13(b)–(c) and in the final column of Table I.

IV. Beyond 100 mW Emission

The performance improvement brought by the donut VCSEL becomes even more interesting for further power scaling.

As discussed previously, self-heating is the critical aspect for reaching higher powers. The homogeneous Dirichlet boundary condition imposed at the bottom of the substrate, representing the heat sink, constrains the peak self-heating temperature once the donut diameter becomes large enough to be comparable with the substrate thickness (150 μm in the present case). Fig. 14 shows both the peak self-heating temperature behaviour as a function of the donut dimensions for a fixed dissipated power density Fig. 14(a) and the new larger design that we want to target, compared with the manufactured structure Fig. 14(b). The blue dashed vertical line in Fig. 14(a) indicates the manufactured donut VCSEL, which reaches a peak self-heating temperature at rollover of 75 °C. Fixing the dissipated power density at the experimental value of 0.30 mW/μm^2, the temperature reaches a maximum and then saturates slightly below it for larger sizes. In the manufactured donut VCSEL we nearly hit the maximum temperature. As shown by our thermal simulations, any larger donut will feature a similar temperature peak, preserving similar VCSEL performance. This result is encouraging for power scaling and, to our knowledge, has not been reported previously.

Stimulated by this evidence, we target a donut size 5 times larger than the manufactured VCSEL, with $D = 150\,\mu$m and $w = 4\,\mu$m (active area of 1885 μm^2). The red vertical line in

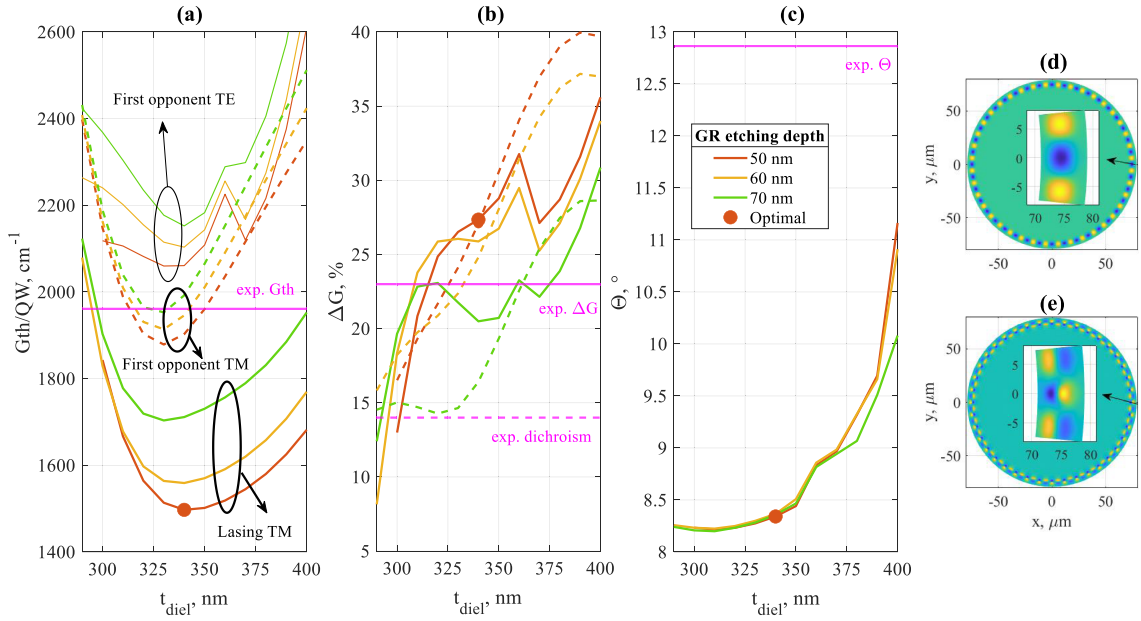


Fig. 15. VELMS simulation results on the large donut aperture. (a): Threshold gain per QW of the targeted mode with the desired TM linear polarisation (thick solid lines), of the same mode with the unwanted TE polarisation (thin lines) and of the first TM-polarised opponent mode (dashed lines) as a function of t_{diel} and t_{etch}. (b) Corresponding relative threshold gain difference ΔG between the targeted TM-mode and the first TM-polarised opponent mode (solid lines) and between both polarisations of the targeted mode, *i.e.*, dichroism (dashed lines). (c) Θ of the targeted TM-mode. Graphs (a), (b) and (c) share the same legend, reported in the (c) panel. In all of the figures, the magenta lines refer to the corresponding simulated quantities for the experimental design. (d) Targeted TM-mode field and (e) first competing TM mode, at the QW.

Fig. 14(a) highlights the corresponding temperature increase, which compares with that of the manufactured donut (blue line) within less than 10°C. With the reasonable assumption that the optical power at rollover scales linearly with the active area, this should lead to 5 times the experimental SPM power of 27 mW, reported in Fig. 11(a). Accounting for a possible earlier rollover related to the slightly higher temperature peak, single-mode output beyond 100 mW might be expected.

After addressing self-heating issues, we now focus on the optical design. For the manufactured device ($D = 30\,\mu$m), the 28-peak whispering-gallery mode was selected using 14 alternated GR regions and rephasing elements. The corresponding geometry is shown again in Fig. 14(b) for comparison with the new power-scaling design, which is not a simple enlarged replica of the original structure.

A purely linear scaling of the manufactured device would require targeting a mode with 28×5 peaks, since the radius is increased by a factor of five. However, our simulations show that selecting a modal order lower than that predicted by strict geometric scaling results in a narrower FF. At the same time, the modal order cannot be reduced arbitrarily, as this would increase the risk of modal competition with modes exhibiting multiple peaks within each GR. A trade-off between far-field narrowing and modal stability is therefore required.

This balance is achieved by targeting an 80-peak whispering-gallery mode. Consequently, the relief pitch is increased, and the lower-than-scaled modal order explains the different azimuthal elongation of the reliefs highlighted in Fig. 14(b) (red ellipses).

In what follows, we first reconsider the GR parameters. The manufactured DC is 38% and proved to work well in maintaining polarisation, but VELMS simulations indicate that 50% would improve the dichroism. At the same time, VELMS predicts a lower G_{th}, which is very beneficial for reducing the dissipated power by lowering the non-radiative carrier recombination rates. With this new grating design, we optimise the other sensitive parameters, namely t_{PML}, t_{etch}, and t_{diel}. After a preliminary simulation campaign, a cap layer thickness of $t_{\text{PML}} = 95$ nm is identified, which is very close to the manufactured value of 100 nm. The relevant figures of merit, *i.e.*, the threshold gain and the dichroism, exhibit low sensitivity on t_{PML}, such that a ± 5 nm range still ensures a satisfactory operation. Then, a joint optimisation of t_{etch} and t_{diel} is performed by VELMS, including the 3D thermal profile, peaked at 83 °C in the active area. The results in terms of threshold gain, modal selectivity and FF properties are detailed in Fig. 15.

In Fig. 15(a), we report the threshold gain G_1 of the targeted TM-mode (thick solid lines), *i.e.*, the one with polarisation perpendicular to the grating bars. At the same time, we show the threshold gain G_1' of the corresponding TE-polarisation (thin solid lines), which should be suppressed, and G_2, the first opponent TM-mode (dashed lines), which represents the most critical source of modal competition. Given two threshold gains, we define a relative threshold gain difference as $\Delta G = (G_2 - G_1)/G_1$. This parameter is relevant both for transverse and polarisation modes, *i.e.*, between the targeted TM-mode and the first competing TM-mode, ΔG, and between the targeted TM- and TE-modes, the dichroism. The corresponding results are reported in Fig. 15(b).

Using (1), we define the FF width Θ as the polar-angle for which the integrated far-field intensity satisfies $\mathcal{I}(\Theta) = 1 - 1/e^2$. Since the integrated FF approaches unity when integrated over the entire angular span, this definition identifies the angular

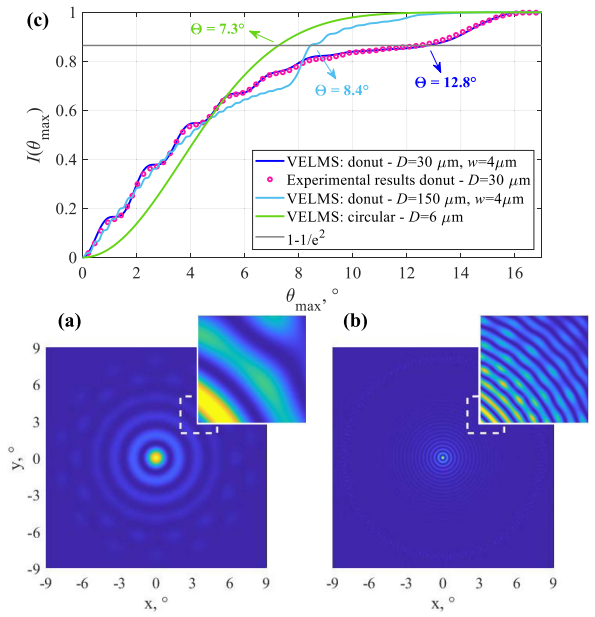


Fig. 16. FF intensity patterns in the donut aperture VCSELs at 80 °C of peak self-heating temperature. (a)–(b) Simulated FF pattern of the small and large donut aperture, respectively. The latter features $t_{\text{diel}} = 340$ nm and $t_{\text{etch}} = 50$ nm. (c) $\mathcal{I}(\theta_{\text{max}})$ for the structures under analysis, including the experimental data coming from the smaller donut. A circular aperture with $D = 6\,\mu$m is reported for comparison. The black horizontal line indicates the $(1 - 1/e^2)$ level.

aperture containing $1 - 1/e^2$ of the total emitted power. The parameter Θ is reported for the targeted TM-mode in Fig. 15(c).

As a reference, the simulated values corresponding to the manufactured VCSEL are indicated by horizontal magenta lines in Fig. 15. In comparison, our optimised device should perform equally or better. For the threshold gain of the targeted mode, we require it to be at least as small as the "experimental value". Concerning the ΔG and dichroism, we instead require the opposite, *i.e.*, that they must be equal to or larger than the reference values.

Eventually, the optimal configuration is identified with $t_{\text{diel}} = 340$ nm and $t_{\text{etch}} = 50$ nm. This design exhibits a 35% lower threshold gain for the targeted TM-mode compared to the manufactured VCSEL, so that the threshold current density remains lower than in the experimental case. In addition, this design provides larger dichroism and ΔG and a Θ reduction of 4°. Concerning the targeted TM-mode threshold gain and the dichroism, by adopting a $t_{\text{etch}} = 70$ nm (close to the experimental 75 nm) and $t_{\text{diel}} = 290$ nm, we retrieve values that are similar to the simulated quantities of the manufactured structure, even though we are considering a slightly different GR. Fig. 15(d)–(e) show the targeted whispering-gallery TM-mode with 80 azimuthal peaks and the first competing TM-mode for the selected optimal structure, including a zoomed inset of the transverse field distributions.

As a final step, Fig. 16 focuses on the FF performance of the manufactured and the newly designed $D = 150\,\mu$m donut. First of all, let us focus on a more quantitative comparison between the measured and computed FF of the $D = 30\,\mu$m donut, whose FF profiles are shown in Fig. 11(c)–(d). In the quantitative representation offered in Fig. 16(c), we can better appreciate the excellent agreement between experiment and simulation for $D = 30\,\mu$m. Furthermore, Fig. 16(a)-(b) illustrate their FF, highlighting the tiny size of the central spot for the $D = 150\,\mu$m. This detail is better appreciated in Fig. 16(c), where its narrower width (12.8vs. 8.4°) is put in good evidence. In addition to these features, the figure provides a useful comparison of the FF performance between our donut VCSELs and a reference circular oxide aperture VCSEL with a diameter of 6 μm, chosen as the maximum size for which single-mode emission was stabilized with a surface GR [45]. This performs slightly better in terms of Θ. However, the power distribution vs. θ_{max} strongly differs, being much more collimated at smaller angles ($\theta_{\text{max}} < 4°$) in the case of the donut shape. There may still be unknown applications where such feature can be usefully exploited.

V. Conclusion

In this work, we designed and demonstrated high-power single-polarisation single-mode axial emission from VCSELs operating at 795 nm for atomic pumping in a quantum gyroscope environment. We determined the two most promising oxide aperture geometries: highly elongated rectangles and donuts. To our knowledge, this work provides a further step toward improved heat dissipation and single-mode operation in high-power VCSELs, motivated by a systematic modeling and experimental investigation.

For the rectangle, a maximum SPM power of 13 mW is reached, featuring an axial, but elongated FF pattern [21]. For the donut, the maximum SPM power attains 27 mW, with a centred circularly symmetric FF. This output power is approximately four times higher than the values reported for comparable 850 nm SPM VCSELs.

High power requires large active areas and currents, which typically lead to strong self-heating, which is responsible for the VCSEL rollover. We found that the best thermal performance is achieved by geometries with a large aspect ratio between width and length: the larger, the better. In that way, heat can be dissipated perpendicularly to the short dimension. This led to the choice of donuts. The next important problem is to sustain single-mode operation with such a large active area, which leads to highly multi-mode emission in standard high-power VCSELs.

We computed the 3D thermal profile in the donut VCSEL starting from the experimental dissipated power density and then coupled it to our in-house electromagnetic solver, VELMS, which includes in full the refractive index variations related to the thermal profile. Great attention is devoted to the far-field and its desired axial pattern for the applications. For all considered geometries, we show that a properly engineered rephasing dielectric layer and an array of grating reliefs allow the device to operate in single higher-order mode and to retrieve on-axis emission.

Motivated by this, we provided a perspective on future work toward obtaining the next record: 100 mW CW-SPM on-axis emission VCSELs.

The proposed surface-patterning approach can be applied in any wavelength window. We foresee significant potential for

longer wavelengths, namely 850 and 940 nm. The latter is particularly appealing, as thermal management is much more favourable, exploiting the much higher thermal conductivity of the binary components (GaAs and AlAs). Additional improvements may also arise from a multi-tunnel-junction VCSEL design, commonly employed in high-power Light Detection and Ranging (LiDAR) systems [41]. In this case, the multi-junction architecture enhances the VCSEL internal quantum efficiency by cascading additional active regions, at the cost of higher dissipated power in CW. Combining the multi-junction approach with the one proposed in this paper would yield an additional multiplicative factor (proportional to the number of junctions), provided that pulsed operation is the pumping method of choice. The expected power performance could make large donut VCSELs a possible alternative to PCSELs in some applications [46], [47]. Although not all of the PCSEL features can be replicated, both VCSELs and PCSELs offer pros and cons that can be balanced according to the requirements of the considered application.

References

[1] J. A. Tatum et al., "VCSEL-based interconnects for current and future data centers," *J. Lightw. Technol.*, vol. 33, no. 4, pp. 727–732, Feb. 2015.

[2] C.-T. Tsai et al., "Multi-mode VCSEL chip with high-indium-density InGaAs/AlGaAs quantum-well pairs for QAM-OFDM in multi-mode fiber," *IEEE J. Sel. Topics Quantum Electron.*, vol. 53, no. 4, Aug. 2017, Art. no. 2400608.

[3] N. N. Ledentsov et al., "High speed VCSEL technology and applications," *J. Lightw. Technol.*, vol. 40, pp. 1749–1763, Mar. 2022.

[4] C. Rimoldi et al., "Near-field measurement and four-wave mixing in single-polarization elliptical multimode VCSELs," *J. Opt.*, vol. 8, no. 1, 2026, Art. no. 015002.

[5] X. Chen et al., "Link bandwidth and transmission capability of single-mode multi-aperture vertical-cavity surface-emitting lasers at 100 G/lane and 200 G/lane over multimode fibers," *MDPI Photon.*, vol. 12, no. 2, 2025, Art. no. 147.

[6] F. Piccirillo et al., "Monolithic integration of one VCSEL on a single mode fiber," *Nanophotonics*, vol. 14, no. 14, pp. 2431–2442, 2025.

[7] R. Michalzik, *VCSELs: Fundamentals, Technology and Applications of Vertical-Cavity Surface-Emitting Lasers*. Berlin, Germany: Springer, 2013.

[8] J. Kitching, "Chip-scale atomic devices," *Appl. Phys. Rev.*, vol. 5, 2018, Art. no. 031302.

[9] J. Lindner et al., "Compact VCSEL chips for diverse applications (795 nm to 850 nm)," in *Proc. SPIE*, vol. 13384, pp. 73–81, 2025.

[10] J. M. Brown and T. G. Walker, "Perspective: Practical atom-based quantum sensors," *Phys. Rev. A*, vol. 112, Oct. 2025, Art. no. 040102.

[11] J. Zhao et al., "Reconfigurable beam steering of multimode VCSEL using multifocal metalens based on phase-change material," *Opt. Commun.*, vol. 606, 2026, Art. no. 132599.

[12] S. Gronenborn et al., "High-power VCSELs with a rectangular aperture," *Appl. Phys. B*, vol. 105, pp. 783–792, 2011.

[13] T. Knödl, M. Golling, A. Straub, and K. J. Ebeling, "Multi-diode cascade VCSEL with 130% differential quantum efficiency at CW room temperature operation," *Electron. Lett.*, vol. 37, pp. 31–33, Jan. 2001.

[14] M. M. Dummer, A. Ghods, G. Xu, S. Rothwell, and K. Johnson, "Single-mode multi-junction VCSELs with integrated transverse mode filter," in *Proc. SPIE*, vol. 12439, pp. 58–65, 2023.

[15] G. P. Bava, P. Debernardi, and L. Fratta, "Three-dimensional model for vectorial fields in vertical-cavity surface-emitting lasers," *Phys. Rev. A*, vol. 63, no. 2, 2001, Art. no. 23816.

[16] V. Torrelli, "Vertical-cavity surface-emitting lasers: Computer-aided modal and polarization engineering," Ph.D. dissertation, Politecnico di Torino, Torino, Italy, 2025.

[17] A. Gullino et al., "VCSEL thermal sources: A physics-based simulation approach," in *Proc. Int. Conf. Numer. Simul. Optoelectron. Devices*, 2025, pp. 129–130.

[18] M. G. C. Alasio et al., "Modeling self-heating in high-power non-circular VCSELs," in *Proc. IEEE Photon. Conf.*, Rome, Italy, Nov. 2024, pp. 1–2.

[19] V. Torrelli et al., "Modeling self-heating in high-power single-mode phase-coupled linear VCSEL arrays," *IEEE Photon. J.*, vol. 17, no. 4, Aug. 2025, Art. no. 1502207.

[20] M. D'Alessandro et al., "Design and modeling of asymmetric bow-tie VCSELs for 100 GHz and beyond," *Opt. Exp.*, vol. 34, pp. 7979–7995, Mar. 2026.

[21] J. Lindner et al., "Phase-engineered distributed grating reliefs for high-power single-mode 795-nm VCSELs with on-axis emission," *Opt. Lett.*, vol. 51, pp. 2924–2927, May 2026.

[22] A. Tibaldi, F. Bertazzi, M. Goano, R. Michalzik, and P. Debernardi, "VENUS: A vertical-cavity surface-emitting laser electro-opto-thermal NUmerical simulator," *IEEE J. Sel. Topics Quantum Electron.*, vol. 25, Nov./Dec. 2019, Art. no. 1500212.

[23] P. Debernardi, G. P. Bava, F. Monti di Sopra, and M. B. Willemsen, "Features of vectorial modes in phase-coupled VCSEL arrays: Experiments and theory," *IEEE J. Quantum Electron.*, vol. 39, no. 1, pp. 109–119, Jan. 2003.

[24] S. Gronenborn et al., "Optical modes in a rectangular VCSEL resonator with properties of both Gaussian and fourier modes," *IEEE J. Quantum Electron.*, vol. 48, no. 8, pp. 1040–1044, Aug. 2012.

[25] T. Gründl et al., "Record single-mode, high-power VCSELs by inhibition of spatial hole burning," *IEEE J. Sel. Topics Quantum Electron.*, vol. 19, no. 4, Jul./Aug. 2013, Art. no. 1700913.

[26] M. Wilkens et al., "Highly efficient high-brightness 970-nm ridge waveguide lasers," *IEEE Photon. Technol. Lett.*, vol. 32, no. 7, pp. 406–409, Apr. 2020.

[27] V. Torrelli et al., "High-power emission via large-area VCSELs with single high-order mode operation," *IEEE Photon. J.*, vol. 16, no. 2, Apr. 2024, Art. no. 0600507.

[28] Å. Haglund, J. S. Gustavsson, J. Vukusic, P. Modh, and A. Larsson, "Single fundamental-mode output power exceeding 6 mW from VCSELs with a shallow surface relief," *IEEE Photon. Technol. Lett.*, vol. 16, no. 2, pp. 368–370, Feb. 2004.

[29] J. M. Ostermann, P. Debernardi, C. Jalics, and R. Michalzik, "Shallow surface gratings for high-power VCSELs with one preferred polarization for all modes," *IEEE Photon. Technol. Lett.*, vol. 17, no. 8, pp. 1593–1595, Aug. 2005.

[30] P. Debernardi, A. Kroner, F. Rinaldi, and R. Michalzik, "Surface relief versus standard VCSELs: A comparison between experimental and hot-cavity model results," *IEEE J. Sel. Topics Quantum Electron.*, vol. 15, no. 3, pp. 828–837, May/Jun. 2009.

[31] A.-S. Gadallah et al., "Oblong-shaped VCSELs with pre-defined mode patterns," in *Proc. SPIE*, vol. 6997, pp. 462–470, 2008.

[32] S. Gehrsitz et al., "The refractive index of $Al_xGa_{1-x}As$ below the band gap: Accurate determination and empirical modeling," *J. Appl. Phys.*, vol. 87, no. 13, pp. 7825–7837, 2000.

[33] M. Farzaneh et al., "Temperature profiling of VCSELs by thermoreflectance microscopy," *IEEE Photon. Technol. Lett.*, vol. 19, no. 8, pp. 601–603, Apr. 2007.

[34] V. Torrelli et al., "Elliptical polarization in VCSELs via joint interaction of a tilted sub-wavelength grating and intrinsic semiconductor anisotropies," *Opt. Lett.*, vol. 50, pp. 3082–3085, May 2025.

[35] V. Torrelli et al., "Elliptically polarized light obtained from tilted high-contrast grating VCSELs," *Opt. Lett.*, vol. 51, pp. 29–32, Jan. 2026.

[36] M. Xun, Y. Sun, X. Jiang, R. Zhang, and J. Zhou, "Stable in-phase mode operation in coherent VCSEL array with an integrated phase shifter," *IEEE Trans. Electron Devices*, vol. 67, no. 7, pp. 2819–2824, Jul. 2020.

[37] F. A. I. Chaqmaqchee and J. A. Lott, "Impact of oxide aperture diameter on optical output power, spectral emission, and bandwidth for 980 nm VCSELs," *OSA Continuum*, vol. 3, no. 9, pp. 2602–2613, 2020.

[38] J. S. Gustavsson, J. A. Vukusic, J. Bengtsson, and A. Larsson, "A comprehensive model for the modal dynamics of vertical-cavity surface-emitting lasers," *IEEE J. Quantum Electron.*, vol. 38, no. 2, pp. 203–212, Feb. 2002.

[39] D. L. Huffaker, H. Deng, Q. Deng, and D. G. Deppe, "Ring and stripe oxide-confined vertical-cavity surface-emitting lasers," *Appl. Phys. Lett.*, vol. 69, pp. 3477–3479, 1996.

[40] H. Deng, Q. Deng, and D. G. Deppe, "Native-oxide laterally confined whispering-gallery mode laser with vertical emission," *Appl. Phys. Lett.*, vol. 69, pp. 3120–3122, Nov. 1996.

[41] H. Liu et al., "High performance multi-junction VCSELs for LiDAR applications," in *Proc. SPIE*, vol. 12020, pp. 15–22, 2022.

[42] A. Kroner, I. Kardosh, F. Rinaldi, and R. Michalzik, "Towards VCSEL-based integrated optical traps for biomedical applications," *Electron. Lett.*, vol. 42, no. 2, pp. 93–94, 2006.

[43] F. M. De Sopra et al., "Near-infrared vertical-cavity surface-emitting lasers with 3-MHz linewidth," *IEEE Photon. Technol. Lett.*, vol. 11, no. 12, pp. 1533–1535, Dec. 1999.
[44] R. Michalzik, "VCSEL fundamentals," in *VCSELs*. Cham, Switzerland: Springer, 2012, pp. 19–75.
[45] P. Debernardi, "HOT-VELM: A comprehensive and efficient code for fully vectorial and 3-D hot-cavity VCSEL simulation," *IEEE J. Quantum Electron.*, vol. 45, no. 8, pp. 979–992, Aug. 2009.
[46] S. Noda et al., "High-power and high-beam-quality photonic-crystal surface-emitting lasers: A tutorial," *Adv. Opt. Photon.*, vol. 15, pp. 977–1032, Dec. 2023.
[47] S. Noda et al., "Photonic-crystal surface-emitting lasers," *Nature Rev. Elect. Eng.*, vol. 1, pp. 802–814, 2024.

Valerio Torrelli received the Ph.D. degree in electronics engineering in 2025. He is currently a Researcher with the Department of Electronics and Telecommunications, Politecnico di Torino, Torino, Italy. His research focuses on vertical-cavity surface-emitting lasers (VCSELs), with emphasis on polarisation engineering and single-mode emission.

Alberto Gullino received the Ph.D. degree in electronics engineering from Politecnico di Torino, Torino, Italy, in 2023. He is currently a Researcher with CNR. His research focuses on the multiphysics modeling of vertical-cavity surface-emitting lasers (VCSELs), with emphasis on tunnel junction (TJ) based designs.

Julian Lindner is currently working toward the Ph.D. degree in physics with the Institute of Physics and Astronomy, Technical University of Berlin, Berlin, Germany. Since 2022, he has been with TRUMPF Photonic Components GmbH, Ulm, Germany, in the field of research and development. His research focuses on the novel concepts for extending the performance limits of single-mode VCSELs.

Gabriele Moiso was born in Casale Monferrato (AL), Italy, in 1999. He received the B.Sc. degree in material science from Università di Torino, Torino, Italy, in 2023. He is currently working toward the master's degree in nanotechnologies for ICTs with Politecnico di Torino, Torino, Italy. His research interests include semiconductor materials and optoelectronic devices.

Martino D'Alessandro received the Ph.D. degree in electronics engineering from Politecnico di Torino, Torino, Italy, in 2026. His research focuses on the modeling and design of vertical-cavity surface-emitting lasers, with emphasis on multimode dynamics.

Stephan Gronenborn was born in Bonn, Germany, in 1982. He received the Ph.D. degree in physics in semiconductor laser physics and optical systems from RWTH Aachen, Aachen, Germany, in 2012. Since 2012, he has been with Philips Research, Amsterdam, Netherlands and also with TRUMPF Photonics, Ulm, Germany as an Architect of VCSELS and micro-optics, looking for advanced laser concepts and new applications.

Markus Herper was born in 1981 in Düren, Germany. He received the Ph.D. degree in physics (laser physics) from RWTH Aachen, Aachen, Germany. From 2008 to 2017, he was with Fraunhofer ILT, Aachen, Germany and RWTH Chair for Technology of Optical Systems, Aachen. In 2017, he joined TRUMPF Photonic Components GmbH (formerly, Philips Photonics), Ulm, Germany, where he is currently with R&D. His research interests include VCSEL technology and photonic components.

Tobias Pusch was born in Mölln, Germany, in 1987. He received the doctoral degree in optoelectronics from ULM University, Ulm, Germany, in 2020. Since 2022, he has been with TRUMPF Photonic Components GmbH, Ulm, Germany, where he is currently working as Project Manager, in the field of research and development. His research focuses on novel VCSEL concepts.

Holger Moench received the Ph.D. degree in high energy physics from RWTH Aachen, Aachen, Germany. In 1991, he joined Philips Research. He is currently a Senior Expert with TRUMPF Photonic Components GmbH, Ulm, Germany. His research interests include the integration of semiconductors and opticsand design of advanced VCSEL structures and new applications for optoelectronic systems.

Alberto Tibaldi received the Ph.D. degree in electronics engineering from Politecnico di Torino, Turin, Italy, in 2015. He is currently an Associate Professor with the Department of Electronics and Telecommunications, Politecnico di Torino. His research focuses on the electro-opto-thermal computer-aided engineering of electronics devices.

Francesco Bertazzi received the Ph.D. degree in electronics engineering from Politecnico di Torino, Turin, Italy, in 2003. He is currently a Full Professor with the Department of Electronics and Telecommunications, Politecnico di Torino. His research focuses on the nonequilibrium Green's function modeling of carrier transport and recombination processes in optoelectronic devices.

Michele Goano (Senior Member, IEEE) received the Ph.D. degree in electronic engineering from Politecnico di Torino, Turin, Italy, in 1993. He is currently a Full Professor with the Department of Electronics and Telecommunications, Politecnico di Torino. His research focuses on the simulation of optoelectronic devices based on narrow- and wide-bandgap semiconductor materials.

Matteo C. G. Alasio (Member, IEEE) received the Ph.D. in electronics engineering from Politecnico di Torino, Torino, Italy, in 2024. He is currently an Assistant Professor with Politecnico di Torino. His research interests include semiconductor device modeling and the development of innovative semiconductor and photonic technologies using both traditional and physics-based AI methods.

Pierluigi Debernardi received the degree in electronics engineering from Politecnico di Torino, Turin, Italy. He is currently the Director of research with CNR. His research interests include the modeling of semiconductor materials and optoelectronic devices and modeling and designing VCSEL structures with non-circular and/or complex geometries, so as to achieve new and specific performances.

Open Access provided by 'Politecnico di Torino' within the CRUI CARE Agreement